Electrochemical Thermal-Mechanical Modelling of Stress Inhomogeneity in Lithium-Ion Pouch Cells

Weilong Ai, [ORCID][1,2] **Ludwig Kraft,** [ORCID][3,*] **Johannes Sturm,** [ORCID][3] **Andreas Jossen,** [ORCID][3] **and Billy Wu** [ORCID][1,2,z]

[1]*Dyson School of Design Engineering, Imperial College London, United Kingdom*
[2]*The Faraday Institution, Quad One, Harwell Science and Innovation Campus, Didcot, United Kingdom*
[3]*Institute for Electrical Energy Storage Technology, Technical University of Munich (TUM), Munich, Germany*

Whilst extensive research has been conducted on the effects of temperature in lithium-ion batteries, mechanical effects have not received as much attention despite their importance. In this work, the stress response in electrode particles is investigated through a pseudo-2D model with mechanically coupled diffusion physics. This model can predict the voltage, temperature and thickness change for a lithium cobalt oxide-graphite pouch cell agreeing well with experimental results. Simulations show that the stress level is overestimated by up to 50% using the standard pseudo-2D model (without stress enhanced diffusion), and stresses can accelerate the diffusion in solid phases and increase the discharge cell capacity by 5.4%. The evolution of stresses inside electrode particles and the stress inhomogeneity through the battery electrode have been illustrated. The stress level is determined by the gradients of lithium concentration, and large stresses are generated at the electrode-separator interface when high C-rates are applied, e.g. fast charging. The results can explain the experimental results of particle fragmentation close to the separator and provide novel insights to understand the local aging behaviors of battery cells and to inform improved battery control algorithms for longer lifetimes.

Lithium-ion batteries with high energy densities are desired to meet the increasing demands for energy storage in electronic devices and electric vehicles. However, electrode materials typically suffer from large volumetric changes during cycling and subsequently large stresses.[1] Silicon, for instance, has a typical volume change of up to 300% during intercalation[2–4] and graphite has a volume expansion of approximately 10%.[5] The resulting stresses can cause surface and intergranular cracking, leading to pulverisation of electrode particles and creation of new surfaces for the formation and growth of the solid-electrolyte interphase (SEI) layer.[6–8] Consequently, this leads to capacity and power fade. These mechanical degradation mechanisms have been found to be strongly coupled with chemical degradation and have great influence on the cycle lifetime of lithium-ion batteries.[9–11] Therefore, it is important to incorporate mechanical effects into electrochemical models of lithium-ion batteries in order to develop advanced battery control algorithms.

Numerous studies have investigated the coupled electrochemical and mechanical behaviors of lithium-ion batteries from particle to cell level, as shown in reviews by McDowell et al.[12] and Zhao et al.[13] Notable works include a mathematical model based on transport and elasticity for volume expansion and stress generation in electrode particles developed by Christensen and Newman[14,15] and a numerical model for intercalation induced stress proposed by Zhang et al.,[16] where a stress field is generated due to the displacement of host atoms caused by the intercalation of lithium-ions. The stress field adds pressure to the crystal structure of the host material, affects the electrochemical potential energy gradient (the driving force of diffusion) and accelerates the solid-state diffusion of ions in the electrode material.[17] The magnitude of stresses in the electrode particles increases with the reaction current density and is affected by battery parameters including particle size and elastic properties, diffusion coefficient and lithium partial molar volume, with maps demonstrating their relationship shown by Purkayastha et al.[18] Large stresses in electrode particles can lead to crack initiation and propagation during lithium-ion insertion and extraction.[19] The stress level in spherical electrode particles can be minimised by choosing the right charging strategy between potentiostatic and galvanostatic conditions,[20] or using optimal charging profiles.[21] The mechanical model for electrode particles is based

on assumptions such as ideally spherical geometry, isotropic properties and free of traction at the surface, but the practical situations inside battery cells are more complex. A computational model was constructed from realistic microstructures of electrode particles in the literature,[22,23] results of which show a strong inhomogeneity in lithium concentration distribution under high C-rates and large stresses in the concave regions of electrode materials. Surface tension and stress can also significantly affect the magnitude and distribution of stresses in electrode particles with small sizes,[24] and the tendency of particle cracking caused by tensile stresses can be reduced by decreasing the particle radius.[2] Furthermore, the volume change of active materials can affect the porosity of electrodes and result in large stresses and additional ionic transport resistance, which can lead to premature failure of batteries.[25]

At cell level, current research works are mainly focused on the electrochemical behaviors of batteries,[26–30] while studies on mechanically coupled battery models are more limited. Notable efforts toward mechanical coupling include Christensen,[31] who applied diffusion-induced stress generation into a porous electrode model for a lithium-ion battery with the results showing that the mechanical effects have a limited influence on the galvanostatic voltage response of discharge for low C-rates but are important for the stress response. Here, large stresses were found near the electrode-separator interface leading to local particle fragmentation,[31] however, coupled thermal effects were not investigated. Later, thermal effects were introduced into the cell model by Fu et al.,[32] who modelled the thickness change of a pouch cell by considering thermal expansion and volume swelling by lithium intercalation. A lithium concentration dependent volume change in graphite particles was used by Rieger et al.[33] to achieve a nonlinear volume expansion with respect to the state of charge, showing good agreement with experimental results. The effects of different anode parameters including porosity and tortuosity on stresses and capacity fade have also been discussed in the literature,[34,35] where anodes with smaller porosities and larger tortuosities show a significant reduction in discharge capacity and larger peak stresses. The hydrostatic stress in electrode particles also has a great influence on the overpotential with a difference of around 20%, according to the multiscale modelling activities by Wu and Lu,[36] and the interaction between electrode particles can lead to large stresses in the binders.

Mechanically coupled battery models can also help to understand the local behaviors of large format lithium-ion batteries. For instance, tab placement has a large impact on the heterogeneity of temperature,

displacement and stress, thus leading to uneven aging behavior as shown by Rieger et al.[37] For pouch cells under fast charging, a fraction of particles (around 35%) close to the separator was found to be fractured as observed from the cross-sectional scanning electron microscopy images of a laptop battery cell.[31] However, the phenomena of stress inhomogeneity in lithium-ion batteries and their effects on battery performance need further elaboration. Properties including current density, particle size, solid phase diffusivity and partial molar volume have been shown in Christensen and Newman[15,31] to have great influence on the peak stress in batteries, while less attention was made on the stress distribution inside electrodes for different C-rates, as well as the thickness change of cells. Fu et al.[32] studied the stress distribution in batteries under different C-rates for power cells and found the impact of stress coupled diffusion on discharge capacity is negligible, but the situation differs for energy cells which have thicker cathodes and are more likely to have stress inhomogeneity. In this work, a pseudo-2D (P2D) battery cell model has been used to study the distributions of stresses in electrode particles and along the cross-section of battery cells. A mechanical model has been incorporated into the electrochemical model, which can give predictions of voltage, temperature, thickness change and stress distribution, and a lumped thermal model is used to describe the bulk temperature. The evolution of stresses in electrode particles under cycling has been calculated at different locations, which can provide an illustration of stress inhomogeneity in battery electrodes. The relationship between the magnitude of stress and C-rates has been studied. The numerical results present a discussion on stress inhomogeneity in battery cells, which is one main reason of the local aging behaviors of batteries.

Electrochemical Model

A variety of simulation models have been developed in the past[38,39] describing different length scales and different physics in lithium-ion batteries. For electrical-thermal state estimation in battery management systems, equivalent circuit models (ECM)[40,41] appear to be fast, accurate and favourable to parameterise, which have been used to simulate global battery states such as cell voltage and temperature in an embedded system. However, those models have difficulties in capturing electrochemical phenomena inside cells, e.g. charge transfer and lithium-ion diffusion. In contrast, the electrochemical models from Newman and co-workers[14,42,43] can provide a detailed description of the physical processes occurring inside the cell. These models have a range of different levels of complexity including 3D,[44] 2D,[45] pseudo-2D (P2D)[26,46] and single particle model,[47] with selection based on the required accuracy. 2D/3D models can consider the cell geometries and the effect on battery performance but come at high computational expense. The single particle model uses only one spherical particle to represent each electrode which results in fast computation. Yet it does not capture lithium-ion concentration gradients across the cell which is problematic when high C-rates are applied, however efforts of increasing the accuracy have been made by combining this with a polynomial profile for lithium-ion concentrations and potentials in the electrolyte.[48] The P2D model uses a set of spherical particles in the two electrodes to ensure accurate prediction of the concentration gradients and is employed in this work to study the stress distribution in electrode particles and across the battery thickness.

Pseudo-2D model.—A schematic of the P2D model is shown in Figure 1, which includes a single layer of cathode, separator and anode with thickness L_p, L_{sep} and L_n respectively, $L = L_p + L_{sep} + L_n$. The entire cell is represented by this 1D structure, while the other spatial directions are assumed homogeneous. The current collectors are considered to have no potential drop due to their high electrical conductivity. The phase potentials ϕ_e and ϕ_s are governed by two charge conservation equations, and the lithium concentrations c_e and c_s are governed by two species conservation equations, where the subscripts "s" and "e" represent the electrode and electrolyte phase, respectively. The four equations are coupled by the Butler-Volmer equation, which defines the reaction current density at the interface between the electrode
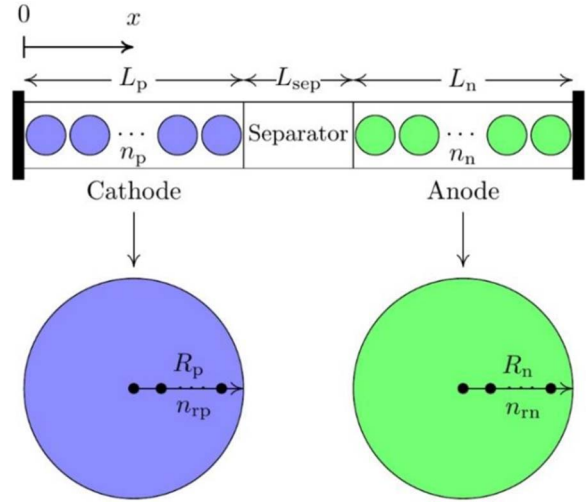

Figure 1. Schematic configuration of the pseudo-2D model for a battery cell.

and electrolyte. These four equations are solved by LIONSIMBA[49] using the finite volume method, and the discontinuities at the interface between the electrodes and the separator are handled by the harmonic mean approach, details of which are given in Appendix A. The electrode particles are assumed to be homogeneously distributed and perfectly spherical, with the number of particles n_p in the cathode and n_n in the anode. The domain inside the electrode particles is locally discretised by a set of points at the particle scale, with the number of points n_{rp} in the cathode and n_{rn} in the anode. The governing equations are summarised in Table I, with full details described in the literature.[42,43,46,49] For ease of demonstration, the coordinates in electrodes are normalised with

$$\bar{x}_p = \frac{x}{L_p} \text{ and } \bar{x}_n = \frac{x - L_p - L_{sep}}{L_n} \quad [1]$$

Lumped thermal model.—The physicochemical material properties for battery materials have a strong temperature dependence, e.g. the charge transfer resistance is known to have a strong correlation with temperature, decreasing exponentially with increasing temperature.[50] An Arrhenius equation[26,46] is typically used to define the thermal sensitivity of physicochemical material properties as

$$\Psi = \Psi_{ref} \exp\left[\frac{E_{act}^{\Psi}}{R}\left(\frac{1}{T_{ref}} - \frac{1}{T}\right)\right] \quad [2]$$

where T is the absolute temperature, R is the universal gas constant, Ψ is one property of interest (e.g. the effective solid phase diffusivity D_s^{eff} and the exchange current density i_0), Ψ_{ref} is the property at the reference temperature T_{ref} with $T_{ref} = 298.15$ K in this work and E_{act}^{Ψ} is the activation energy with respect to Ψ.

The heat balance of the cell[33] can be stated as

$$\rho_{cell}\, c_{p,cell}\, V_{cell}\, \frac{\partial T}{\partial t} = q_{tot} - q_{conv} - q_{rad} \quad [3]$$

where ρ_{cell}, $c_{p,\,cell}$ and V_{cell} are the density, heat capacity and volume of the cell, respectively. q_{conv}, q_{rad} and q_{tot} are the dissipated heat by convection and radiation and the averaged heat generation in the cell respectively. They are calculated as

$$q_{conv} = h_{conv}\, A_{cell}\,(T - T_{ref}) \quad [4]$$

$$q_{rad} = \epsilon_{rad}\, \sigma_B\, A_{cell}\,(T^4 - T_{ref}^4) \quad [5]$$

$$q_{tot} = \chi \frac{V_{cell}}{L} \int_0^L \left[i_s \nabla \phi_s + i_e \nabla \phi_e + a_s F\, j^{Li}\left(\eta + T\frac{\partial E_{OCV}}{\partial T}\right)\right] dx \quad [6]$$

where h_{conv} is the convective heat transfer coefficient, ϵ_{rad} is the emissivity, σ_B is the Stefan-Boltzmann constant, a_s is the specific surface to

Table I. P2D electrochemical model equations for lithium-ion batteries.[26]

Conservation equations		Boundary conditions
Species, electrolyte phase	$\epsilon_e \frac{\partial c_e}{\partial t} = \frac{\partial}{\partial x}(D_e^{eff} \frac{\partial c_e}{\partial x}) + \frac{1-t_+}{F} j^{Li}$	$\frac{\partial c_e}{\partial x}\|_{x=0} = \frac{\partial c_e}{\partial x}\|_{x=L} = 0$
Species, solid phase	$\frac{\partial c_s}{\partial t} = \frac{D_s^{eff}}{r^2} \frac{\partial}{\partial r}(r^2 \frac{\partial c_s}{\partial r})$	$\frac{\partial c_s}{\partial r}\|_{r=0} = 0, \;\; D_s^{eff} \frac{\partial c_s}{\partial r}\|_{r=R} = -\frac{j^{Li}}{a_s F}$
Charge, electrolyte phase	$\frac{\partial}{\partial x}(\kappa^{eff} \frac{\partial \phi_e}{\partial x}) + \frac{\partial}{\partial x}(\kappa_D^{eff} \frac{\partial \ln c_e}{\partial x}) + j^{Li} = 0$	$\frac{\partial \phi_e}{\partial x}\|_{x=0} = 0, \;\; \phi_e\|_{x=L} = 0$
Charge, solid phase	$\frac{\partial}{\partial x}(\sigma^{eff} \frac{\partial}{\partial x} \phi_s) = j^{Li}$	$\sigma^{eff} \frac{\partial \phi_s}{\partial x}\|_{x=0} = \sigma^{eff} \frac{\partial \phi_s}{\partial x}\|_{x=L} = I$
		$\sigma^{eff} \frac{\partial \phi_s}{\partial x}\|_{x=L_p} = \sigma^{eff} \frac{\partial \phi_s}{\partial x}\|_{x=L-L_n} = 0$
Butler-Volmer kinetic	$j^{Li} = 2a_s i_0 \sinh(\frac{0.5F}{RT}\eta), \; i_0 = k_i \sqrt{c_e(c_{s,\,max} - c_{s,\,surf})c_{s,\,surf}}$	
Coefficients[49]	$D_e^{eff} = \epsilon_e^{brugg} \times 10^{-4} \times 10^{-4.43 - \frac{54}{T - 229 - 5\times10^{-3}c_e} - 0.22\times10^{-3}c_e}$	
	$D_s^{eff} = D_s \times e^{-\frac{5000}{R}(\frac{1}{T} - \frac{1}{T_{ref}})}, \;\; \sigma^{eff} = \epsilon_s \sigma$	
	$\kappa^{eff} = \epsilon_e^{brugg} \times 10^{-4}c_e[-10.5 + 0.688\times10^{-3}c_e + 0.494\times10^{-6}c_e^2 + (0.074 - 1.78\times10^{-5}c_e - 8.86\times10^{-10}c_e^2)T$	
	$\quad + (-6.96\times10^{-5} + 2.8\times10^{-8}c_e)T^2]^2$	
	$\kappa_D^{eff} = \frac{2RT}{F}\kappa^{eff}(1-t_+)(1 + \frac{d \ln f_\pm}{d \ln c_e})$	
	$(1 + \frac{d \ln f_\pm}{d \ln c_e}) = \frac{0.601 - 0.24c_e^{0.5} + 0.982[1 - 0.0052(T - T_{ref})]c_e^{1.5}}{(1 - t_+)}$ [33]	

volume, F is the Faraday constant, E_{OCV} is the thermodynamic equilibrium potential, j^{Li} is the current density and η is the overpotential between solid and liquid phases. A_{cell} and V_{cell} are the surface area and volume of the cell, respectively. Heat generation in the current collector foils is not included, because the heat generation from the ohmic drop in current collectors is assumed negligible. χ is the volume fraction of materials generating heat in the cell, e.g. $\chi = 0.9187$.[33]

In this work, the Enertech lithium cobalt oxide-graphite (LCO-G) SPB655060 pouch cells[33] are used for parameterisation and validation of the model. These cells have a low Biot number (e.g. below the range of 0.1 in the x direction[33]), and thus the impact of thermal gradients within the cell is not considered. In this work, a homogeneous temperature is assumed inside the battery cells. The temperature is calculated by the lumped thermal model, and the thermal gradients in electrode particles are neglected.

Mechanical Model

A stress model for a single electrode particle has been proposed by Christensen and Newman,[14,15] based on theories of transport and elasticity in diffusion. Alternatively, an intercalation-induced stress model has been developed by Zhang et al.[16] for electrode particles and has been used in the SPM for battery modelling.[51] Here, this model is applied to a P2D model to study the stress inhomogeneity in battery cells. The solutions of stress distribution and displacement in electrode particles are briefly introduced below, while details are referred to Zhang et al.[16] The mechanical governing equations for an ideal spherical particle, with a radius R_i, are summarised in Table II. The parameters E and v are Young's modulus and Poisson's ratio, respectively. ε_r, ε_θ, σ_r and σ_θ are strains and stresses in radial and tangential directions respectively, with r and θ denoting two spherical coordinates originated at the particle centre. Here strain is coupled with lithium concentration using an analogical law to thermal strain,[16] where Ω is the partial molar volume of solute and $\bar{c} = c - c_0$ with c_0 being the reference concentration.

The analytical solution of stresses and displacement is presented by Zhang et al.[16] as

$$\sigma_r(r) = \frac{2\Omega E}{3(1-v)}\left(\frac{1}{R_i^3}\int_0^{R_i} \bar{c}r^2 dr - \frac{1}{r^3}\int_0^r \bar{c}r^2 dr\right) \quad [7]$$

$$\sigma_\theta(r) = \frac{\Omega E}{3(1-v)}\left(\frac{2}{R_i^3}\int_0^{R_i} \bar{c}r^2 dr + \frac{1}{r^3}\int_0^r \bar{c}r^2 dr - \bar{c}\right) \quad [8]$$

$$u(r) = \frac{\Omega}{3}\frac{1+v}{1-v}\frac{1}{r^2}\int_0^r \bar{c}r^2 dr + \frac{2\Omega}{3}\frac{1-2v}{1-v}\frac{r}{R_i^3}\int_0^{R_i} \bar{c}r^2 dr \quad [9]$$

The radius change of particles after lithium intercalation or extraction can be estimated by defining $r = R_i$ in Equation 9

$$dR_i = u(R_i) = \frac{\Omega R_i}{3}\frac{3}{R_i^3}\int_0^{R_i} \bar{c}r^2 dr = \frac{\Omega R_i}{3}\bar{c}_{avg} \quad [10]$$

where $\bar{c}_{avg}$ is the average concentration of intercalated lithium in the electrode particle.

This solution indicates the relationship between lithium concentration, volume change and stress with the below assumptions:

• the volume change of electrode particles is determined by the average concentration of intercalated lithium.
• the magnitude of stresses is determined by the inhomogeneity level of lithium concentration.

Stress coupled diffusion.—The mechanical model highlights the role of lithium concentration gradients as a driving force for stresses in electrode particles. However, it is also important to consider that the stresses also affect the intercalation process and concentration distribution within electrode particles.[51] Zhang et al.[16] introduced the mechanical strain energy to the electrochemical potential for a solid solute and modified the species diffusion equation in electrode

Table II. Mechanical governing equations for spherical electrode particles.

Equilibrium of stresses	$\frac{d\sigma_r}{dr} + \frac{2}{r}(\sigma_r - \sigma_\theta) = 0$
Boundary conditions	$\frac{d\sigma_r}{dr}\|_{r=0} = 0, \; \sigma_r\|_{r=R_i} = 0$
Constitutive equation	$\varepsilon_r = \frac{1}{E}(\sigma_r - 2v\sigma_\theta) + \frac{\Omega}{3}\bar{c}, \; \varepsilon_\theta = \frac{1}{E}[\sigma_\theta - v(\sigma_r + \sigma_\theta)] + \frac{\Omega}{3}\bar{c}$
Compatibility condition	$\varepsilon_r = \frac{du}{dr}, \; \varepsilon_\theta = \frac{u}{r}$

particles to

$$\frac{dc}{dt} = D\left[\frac{d^2c}{dr^2} + \frac{2}{r}\frac{dc}{dr} + \theta_M\left(\frac{dc}{dr}\right)^2 + \theta_M\bar{c}\left(\frac{d^2c}{dr^2} + \frac{2}{r}\frac{dc}{dr}\right)\right] \quad [11]$$

where $\theta_M = \frac{\Omega}{RT}\frac{2\Omega E}{9(1-\nu)}$. The boundary conditions for electrode particles in Table II are thus changed to

$$\left.\frac{\partial c}{\partial r}\right|_{r=0} = 0, \quad (1 + \theta_M\bar{c})D_s^{\text{eff}}\left.\frac{\partial c}{\partial r}\right|_{r=R} = -\frac{j^{\text{Li}}}{a_s F} \quad [12]$$

When $\theta_M = 0$, there are no mechanical effects on the diffusion of species in electrodes and Equation 11 returns to the standard equation in the Newman's model in Table I; otherwise the physics of stress coupled diffusion is enabled.

Thickness change.—The thickness change of a battery consists of two contributions: thermal expansion and expansion due to lithium (de)intercalation. Since a lumped thermal model is used, the thickness change by thermal expansion is determined by using the average temperature

$$dL_{\text{th}} = \alpha_{\text{cell}}(T - T_{\text{ref}}) \quad [13]$$

where the thermal expansion coefficient is a constant with $\alpha_{\text{cell}} = 1.1\ \mu\text{m/K}$.[33] The thickness change by lithium intercalation originates from the change of crystal structure and lattice spacing of active materials. Considering the thickness of the anode and cathode layers is much smaller than the length and width of the cell, the thickness change is estimated by the volume change[33] as

$$\frac{dL}{L} \approx \epsilon_s\frac{dV}{V} \quad [14]$$

where ϵ_s is the volume fraction of the active materials. Since the P2D model is based on spherical particles, the volume change is estimated using Equation 10 as

$$\frac{dV_i}{V_i} = \frac{\frac{4}{3}\pi(R_i + dR_i)^3 - \frac{4}{3}\pi(R_i)^3}{\frac{4}{3}\pi R_i^3} \approx \frac{3dR_i}{R_i} = \Omega\, c_{i,\text{avg}} \quad [15]$$

Substituting Equation 15 to Equation 14, the thickness change by lithium intercalation is

$$dL_{\text{int}} = n \cdot \sum_{i=1}^{n_p+n_n} dL_i = n \cdot \sum_{i=1}^{n_p+n_n} \epsilon_s\,\Omega\, c_{i,\text{avg}}L_i \quad [16]$$

where L_i is the thickness of the layer fraction represented by the particle, and n is the number of anode and cathode layers in the pouch cell. The thickness change of the cell in total is

$$dL = dL_{\text{th}} + dL_{\text{int}} = \alpha_{\text{cell}}(T - T_0) + n \cdot \sum_{i=1}^{n_p+n_n} \epsilon_s\,\Omega\, c_{i,\text{avg}}L_i \quad [17]$$

Validation and Analysis

A study on voltage and stress responses of batteries has been carried out under various C-rates using the P2D model. The model is based on the open-source LIONSIMBA platform,[49] with a modified algorithm for diffusion in electrode phases to consider the influence of mechanical effects. Parameters are based on the Enertech LCO-G SPB655060 pouch cell[33,52] and are presented in Table III unless stated otherwise. Curves of open circuit voltage (OCV) and entropy for LCO and graphite are taken from literature.[33] For validation of the model, the sensitivity of discretisation was tested by changing the number of electrode particles in the battery cross section and the number of points inside electrode particles. Then the simulation results by the proposed model were compared with the experimental results by Rieger et al.[33] After validation, the mechanical effects on battery performance are discussed, where the stress profiles in electrode particles were obtained under different C-rates of discharge and cycling. In Subsections 4.3−4.5 for the stress analysis, the cell temperature was maintained at the ambient temperature T_{ref} to eliminate the thermal effects on stresses. The stress distribution over the battery cross-section was calculated under different C-rates of discharging, which showed the stress inhomogeneity in battery cells for high C-rates.

Test of discretisation.—In LIONSIMBA,[49] the finite volume method and the finite difference method are used to discretise the spatial domain over the battery cross-section and inside electrode particles respectively. The accuracy of calculation results is dependent on the quality of the discretisation, and for high C-rates of currents, a

Table III. Parameters for Enertech LCO-G SPB655060 pouch cell.[33,56]

| Parameter	Cathode (LiCoO$_2$)	Separator	Anode (LiC$_6$)
Thickness t (μm)	68	25	76.5
Particle radius R_i (μm)	3		5
Active material fraction ϵ_s	0.62		0.61
Porosity ϵ_e	0.32	0.5	0.33
Bruggeman's coefficient brugg	1.83	1.5	2.914
Maximum concentration $c_{s,\text{max}}$ (mol m^{-3})	49943		29700
Stoichiometric coefficients (fully charged)	0.435		0.84
Stoichiometric coefficients (fully discharged)	0.9651		0.0065
Solid diffusivity D_s (m^2 s^{-1})	5.387×10^{-15}		3.9×10^{-14}
Solid conductivity σ (S m^{-1})	10		100
Young's modulus E (GPa)	375		15[57]
Poisson's ratio	0.2[58]		0.3[57]
Partial molar volume (cm^3 mol^{-1})	−0.728		3.1[57]
Parameter for the whole cell			
Transference number t_+	0.38		
Cell size (mm)	51 × 47 × 6.4		
Cell density ρ_{cell} (g cm^{-3})	2.47		
Cell heat capacity $c_{p,\text{cell}}$ (J kg^{-1} K^{-1})	1080.2		
Heat transfer coefficient h_{conv} (W m^{-2} K^{-1})	35		
Thermal expansion coefficient α_{cell} (μm K^{-1})	1.1		
Emissivity ϵ_{rad}	0.95		
Number of layers n	34		
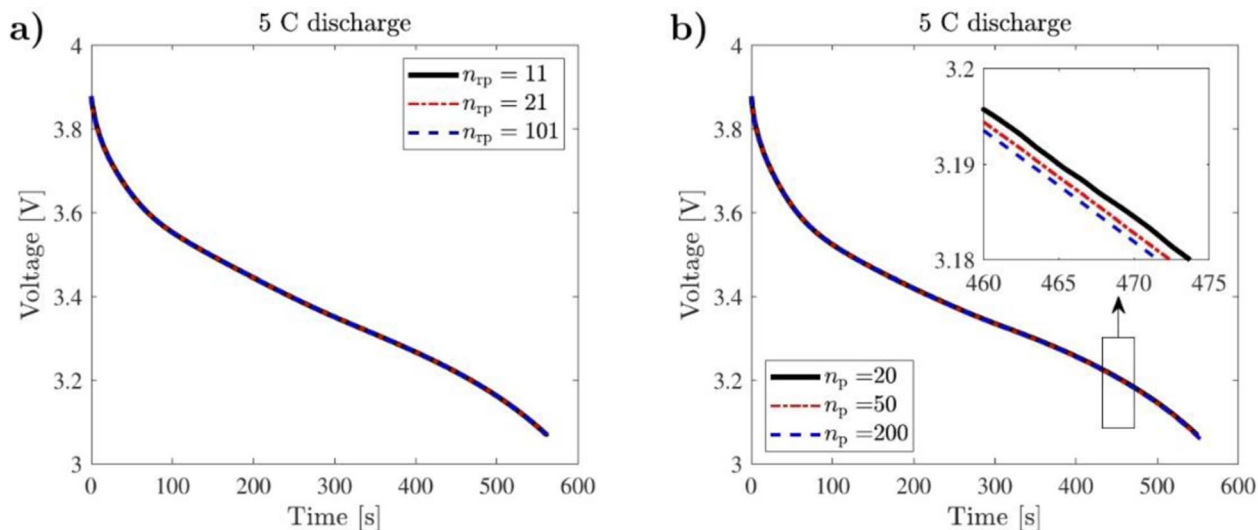
Figure 2. Sensitivity of the discretisation in the P2D model: (a) changing the number of points n_{rp} inside electrode particles; (b) changing the number of volumes n_p in the cross-section of the cell.

large number of volumes and points are required to capture the gradients in concentration and potential. Here a study on the sensitivity of element/point number has been carried out, including two cases in the discretisation: fixing the number of volumes $n_p = 50$ and changing the number of points n_{rp}; and changing n_p and fixing $n_{rp} = 21$. In both cases, the numbers of volumes and points in the cathode are the same as the in anode, i.e. $n_p = n_n$ and $n_{rp} = n_{rn}$. The results in Figure 2 show that the accuracy can be ensured by using $n_{rp} = n_{rn} = 21$ and $n_p = n_n = 50$. The responses of voltage for batteries under different C-rates below 5 C have also been tested, but no significant difference is observed. Here the 1 C current density is 29.2 A/m^2 for the Enertech pouch cells.

Model validation.—The responses of voltage, temperature and thickness change for the Enertech pouch cell under different discharge C-rates have been calculated and compared with the experimental results from Rieger et al.,[33] as shown in Figure 3. The simulation results have been validated for discharge rates up to 2 C, because the cell is designed by the manufacturer to operate in a restricted window: maximum charging rate 1 C and maximum discharging rate 2 C.[33,52] Experiments beyond these restrictions will cause irreparable damage to the cell, so battery cycling for higher C-rates have not been tested in experiments but explored by simulation using the proposed model. Here the temperature rise in Figure 3b is the average temperature of the cell, which is calculated with the lumped thermal model (0D), related to the ambient temperature T_{ref}. A constant thermal expansion coefficient is defined in the simulation, so the thermal expansion curves show similar trends with the temperature curves. The thickness change of the cell is nonlinear with respect to the state of charge in Figure 3c, because a nonlinear volume change in graphite from literature[33] was used, details of which are included in Appendix B. The thermal expansion is calculated using Equation 13. By subtracting the values of thickness change in Figure 3c and thermal expansion in Figure 3d, the thickness change caused by intercalation of lithium-ions can be obtained and is shown to be ten times larger than that of thermal expansion.

Mechanical effects on diffusion.—The effects of stresses on the diffusion in solid phases and the voltage response during discharge have also been studied. Two cases of models without and with mechanical effects are considered, by setting $\theta_M = 0$ and $\theta_M = \frac{\Omega}{RT}\frac{2\Omega E}{9(1-\nu)}$ respectively. Different C-rates have been considered ranging from 0.5 to 5 C, where the rates from 3 to 5 C are above the maximum rate recommended by the manufacturer. The results in

Figures 4a–4b show that mechanical effects make limited contribution to the diffusion and the voltage response for batteries under low C-rates up to 2 C, while mechanical effects become more important for higher C-rates. This is because high C-rates cause large reaction current density variations in the electrode leading to lithium concentration gradients in the solid phase, which then result in large stresses at the electrode particle surfaces. Here, the stress field increases the accessible capacity by up to 5.4% when discharged at 5 C as shown in Figure 4b due to stresses accelerating the lithium diffusion inside electrode particles, Figures 4c–4d.

The distribution of the maximum stress in electrode particles across the battery section is displayed in Figure 5, which shows that the magnitude of stresses in electrode particles increases with the C-rate. The distribution of the maximum tangential stress distribution is almost homogeneous for a 2 C discharge, while large stresses are found close to the separator for a 5 C discharge, in both cathode and anode particles. This figure also shows the original model of diffusion in solid phases without considering the mechanical effects will overestimate the maximum stress level by up to 50%, which is because mechanical stresses accelerate the lithium diffusion in solid phases and reduce the concentration gradients in the modified model as shown in Figure 4c. In contrast, there is little difference in the voltage responses between 'with mechanical effects' and 'without mechanical effects' at 2 C and below, because the surface lithium concentrations between those two models have little difference in Figure 4c, which results in similar OCV values and voltage profiles. The peak stress is close to the separator in Figure 5 because for high C-rates, electrode particles close to the separator have high reaction current densities, leading to large stresses at this region, while reaction current densities at the current collector sides are smaller. As the particles near the electrode-separator interface get increasingly depleted/saturated during discharge, the peak reaction current density propagates deeper into the electrode to cause the stress peaks observed in Figure 5 at approximately $\bar{x}_p = 0.8$ and $\bar{x}_n = 0.4$ during the 5 C discharge.

Stress evolution across battery electrode.—The stresses in the electrode particles have a strong dependence on the lithium concentration gradients, as shown in the theoretical model in Section 0. The impact of cycling on the cell behavior has been explored in Figure 6, where lithium concentration distributions and tangential stress distributions at the specific time steps (marked in Figure 6) are presented in Figure 7 and Figure 8, respectively. Electrode particles at three different locations (close to the current collector, middle point and close to the separator) are plotted out in both cathode and anode, while the other particles are omitted in Figure 7 and Figure 8. A constant
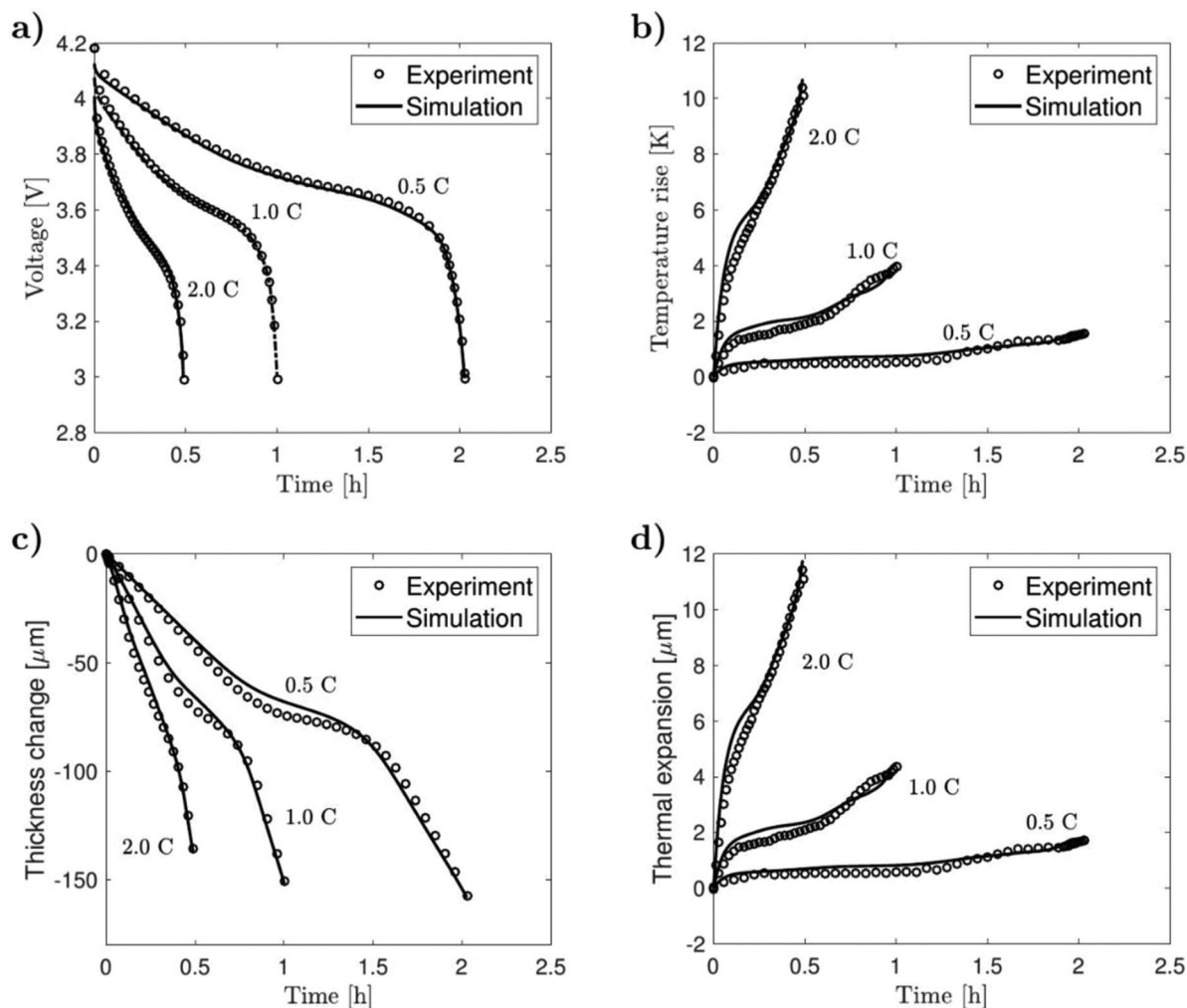
Figure 3. Validation of the model with experimental data from Rieger et al.:[33] (a) voltage; (b) temperature rise; (c) thickness change of the cell; (d) thermal expansion calculated using Equation 13.

current density of 58.4 A/m^2 (2 C) was applied as shown in Figure 6a, and the current direction was reversed to switch between charging and discharging when the voltage reached the operating voltage window limits (between 3 and 4.2 V) in Figure 6b. No degradation was included, so only six cycles were considered.

When the cell starts to discharge from time step a to b, electrode particles close to the separator experience large tangential stress at the surface in Figures 6c–6d. During this time, lithium-ions travel from the anode to the cathode, leading to large lithium concentration gradients in Figure 7b and large stresses in Figure 8b close to the separator. This can be ascribed to the higher reaction current density in these locations caused by the shorter diffusion distance between the anode and cathode particles. As the particles close to the separator charge/discharge faster, (de)intercalation becomes less favourable (Figure 7c) and the peak reaction current density then moves deeper into the electrode at time step c resulting in the stresses close to the separator decrease in Figures 6c–6d. Subsequently, a peak stress wave propagates deeper into the electrode toward the current collectors as can be seen in Figures 8c–8d. By point d in Figure 7, the reaction current density in particles close to the electrode-separator interface has reached its lowest point and lithium concentration gradients have had time to be equalised, resulting in the observed reduction in stress at the end of discharge.

The charging stage is carried out after the cell voltage reaches the cutoff level at the time step d, and lithium-ions are extracted from the cathode and move to the anode, changing the concentration gra-

dient, as shown in Figure 7e. Large compressive tangential stresses are detected close to the separator between time steps d and e in Figures 6c–6d and Figure 8e, due to ease of (de)intercalation and large concentration gradients from the depleted anode and saturated cathode particles at the electrode-separator interface in Figure 7e. When the charging stage terminates at the time step f, lithium concentration gradients in the electrode particles close to the separator reach a minimum value in Figure 7f, leading to small stresses in Figure 8f. This is again due to the propagation of the reaction current density deeper into the electrode during charge caused by depletion/saturation of lithium in the cathode/anode at the particles close to the electrode-separator interface.

In the following discharging process, the concentration distributions in Figures 7g–7h are similar to the results in Figures 7b–7d. Electrode particles close to the separator have larger stresses as shown in Figure 8g, and when the discharging process finishes the current collector sides have larger stresses, see Figure 8h. The results show that the stress distribution is strongly inhomogeneous in the cross-section of the cell, with the maximum stress close to the separator. Electrode particles experience cyclic loading of tensile and compressive stresses, which can cause fatigue crack propagation and create new surfaces for the SEI formation, one main degradation mechanism of lithium-ion batteries.[6] Large tensile stresses are also found at the centre of the electrode particles as presented in Figure 8e, which can lead to particle cracking from the inside.[19] The degradation model caused by stress and crack propagation is under development, and experiments
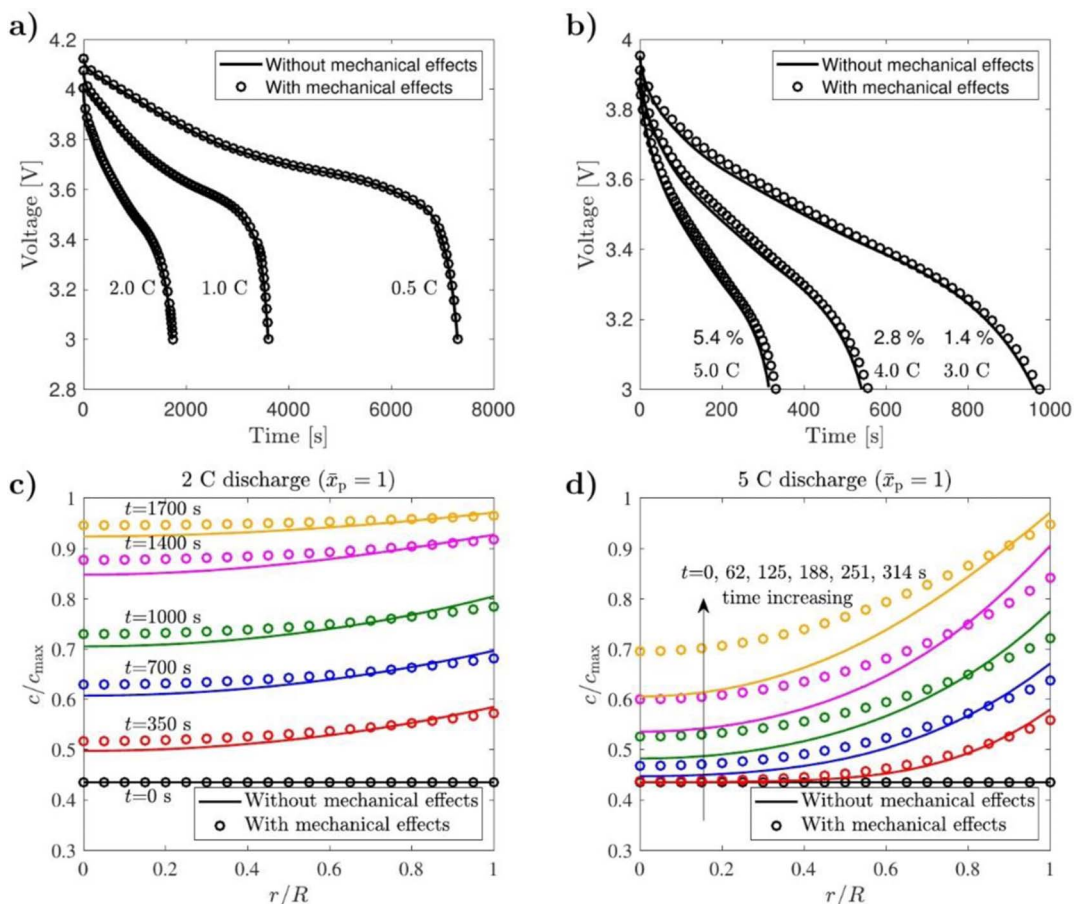
Figure 4. The mechanical effects on the response of battery cells under different C-rates of discharging: (a) low C-rates of 0.5, 1 and 2 C; (b) high C-rates of 3, 4 and 5 C; concentration distribution inside the cathode particle at $\bar{x}_p = 1$ for discharging in (c) 2 C and (d) 5 C.

are planned to study electrode particle cracking for lithium-ion battery cells under high C-rates.

The results in Figure 8 show two kinds of stress in electrode particles under discharge. For anode particles, the outer layer is under tensile tangential stress, while the inner part has compressive tangential stress. Cathode particles show the same stress condition as the anode particles, but the trends are reversed. This is because the cathode material LCO has a negative partial molar volume, i.e. the intercalation

of lithium-ions into the LCO leads to a decrease in its volume.[53] The reverse situation occurs to cathode and anode particles when the cell is charged, as shown in Figures 8e–8f. The status of tangential stress in electrode particles for charging and discharging is summarised in Table IV.

Stress versus C-rates.—The distributions of the maximum tangential stress at particle surface under different C-rates are given in
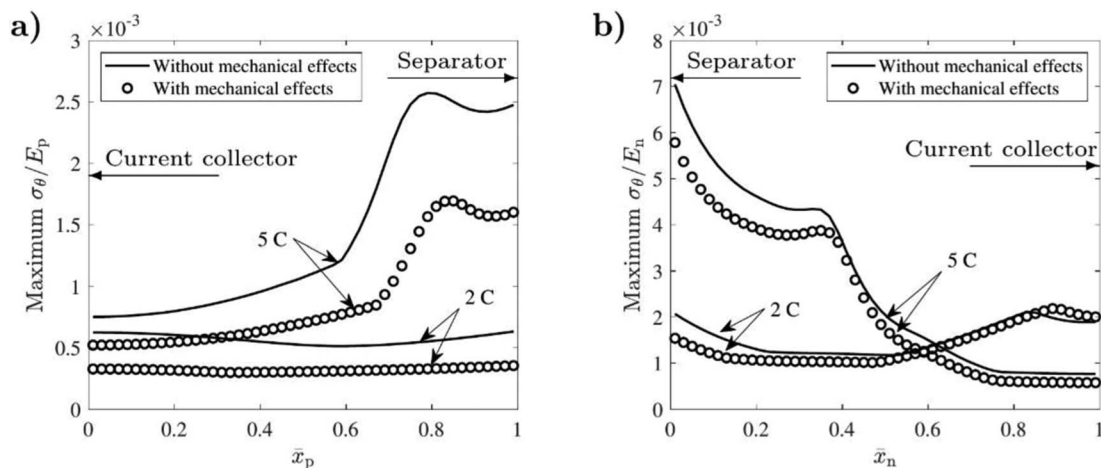

Figure 5. The distribution of the maximum tangential stress in electrode particles across the cell cross-section under 2 and 5 C discharging: (a) cathode; (b) anode.
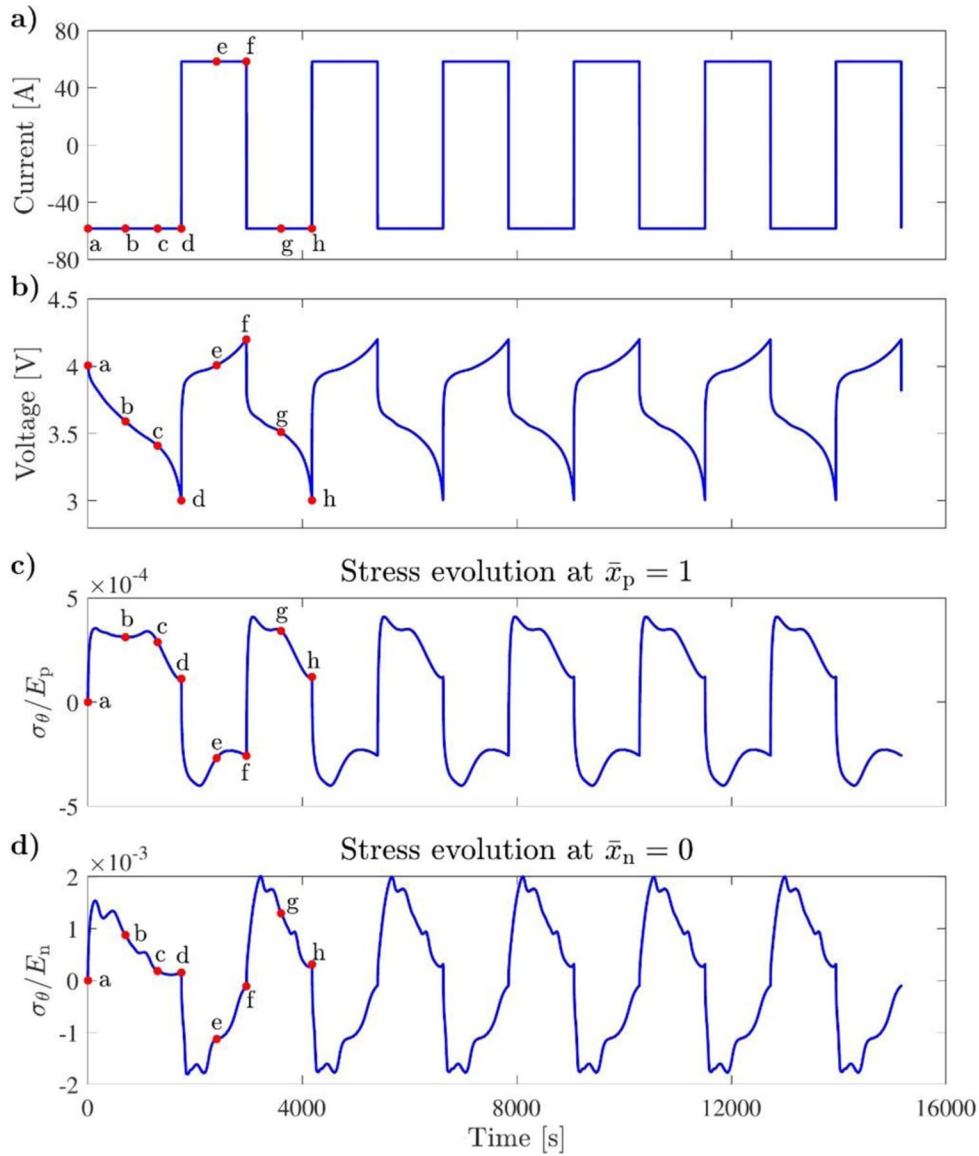
Figure 6. Cycling response of battery cells at 2 C: (a) currents; (b) voltage; tangential stress at the surface of (c) cathode particle at $\bar{x}_p = 1$ and (d) anode particle at $\bar{x}_n = 0$. At the marked time steps, concentration and stress distributions in electrode particles are presented in Figure 7 and Figure 8 respectively.

Figures 9a–9b. Below 1 C, the distribution of tangential stresses is found to be almost homogeneous in both the cathode and anode, while for higher C-rates, large stresses are generated at particles close to the separator in both electrodes, as shown in Figure 9b. The magnitude of tangential stress versus C-rate at different locations is presented in Figures 9c–9d. The tangential stresses generally increase with C-rate, and for particles close to the separator, the relationship is highly non-linear. In contrast, the tangential stress is maintained at particles close to the current collectors for increasing C-rates above 3 C. The large stresses at the separator interface can be explained by considering

that the reaction current density between cathode and anode mainly occurs at particles close to the separator for high C-rates. In return, this leads to high concentration gradients at these locations, while the concentration gradients in particles at the current collectors are low.

Conclusions

A mechanically coupled P2D model has been presented to study the stress heterogeneity in lithium-ion battery electrodes. This model can predict the voltage, temperature and thickness changes for a pouch cell

Table IV Stress status in the cathode and anode particles.

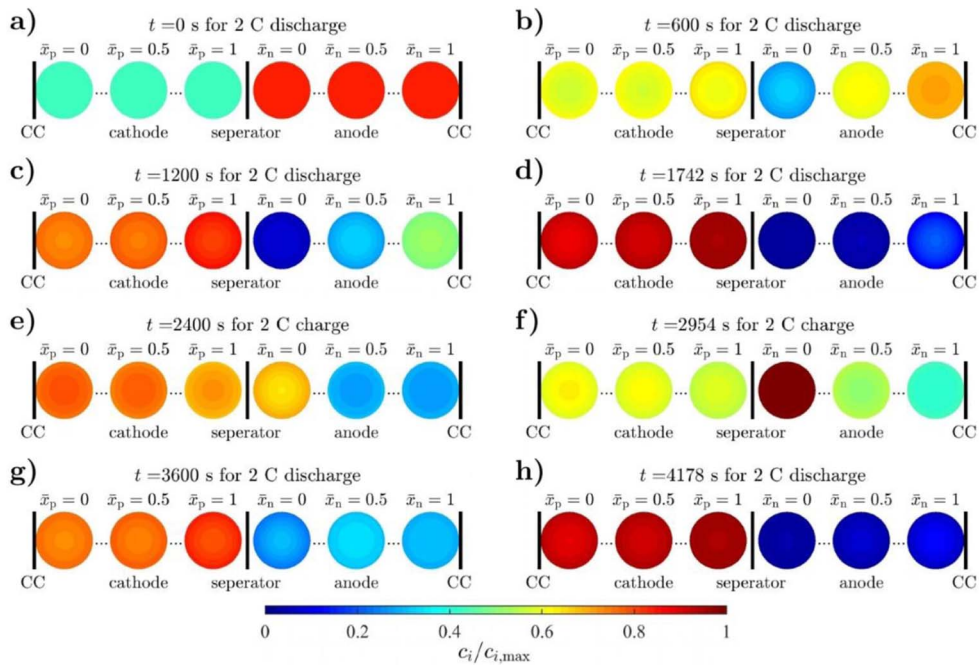| Material property	Cathode particle (LiCoO$_2$) $\Omega < 0$		Anode particle (LiC$_6$) $\Omega > 0$	
Region	$r = 0$	$r = R_p$	$r = 0$	$r = R_n$
Charge	$\sigma_\theta > 0$	$\sigma_\theta < 0$	$\sigma_\theta > 0$	$\sigma_\theta < 0$
Discharge	$\sigma_\theta < 0$	$\sigma_\theta > 0$	$\sigma_\theta < 0$	$\sigma_\theta > 0$

Figure 7. Concentration distribution inside electrode particles at different time steps of 2 C-rate cycling: (a-h) $t = 0$, 600, 1200, 1742, 2400, 2954, 3600 and 4178 s respectively. The subscript $i = $ p or n, representing the cathode or anode domain, respectively. The current collector is abbreviated as CC.

showing good agreements with experimental results, where a lumped thermal model is used to describe thermal variations. The battery performance is affected by the evolving mechanical stresses within the electrode particles. The influence of stress-enhanced diffusion on the discharge capacity is limited for batteries under low C-rates of currents but becomes more important for high C-rates. The diffusion of lithium in solid phases is accelerated by introducing the mechanical effects, otherwise the stress responses in electrode particles are overestimated using the solution of concentration distributions from the standard P2D model.

A cyclic response of tensile and compressive tangential stresses has been modelled at the particle surfaces for batteries under galvanostatic cycling, which can lead to fatigue crack growth/propagation even though the stress level is below the fracture toughness of the material. The magnitude of stresses nonlinearly increases with C-rates at the electrode-separator interface and is maintained at the current collector sides, when high C-rates of currents are applied. These results can explain the experimental results of particle fragments found close to the separator for batteries under fast charging. The proposed model can be used to predict the crack propagation at electrode particles and
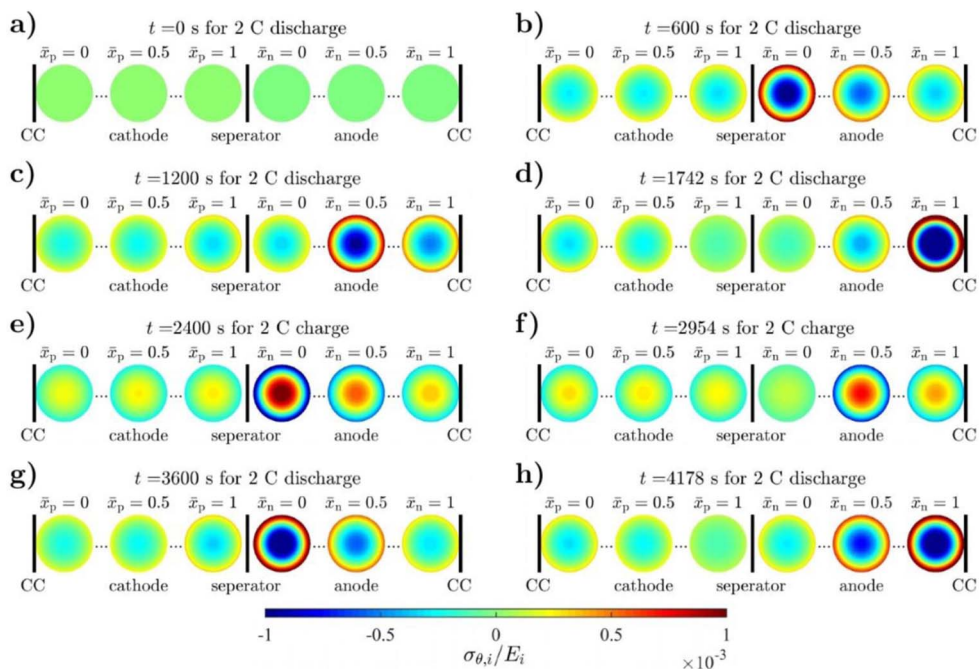

Figure 8. Tangential stress distribution inside electrode particles at different time steps of 2 C-rate cycling: (a-h) $t = 0$, 600, 1200, 1742, 2400, 2954, 3600 and 4178 s respectively. The subscript $i = $ p or n, representing the cathode or anode domain, respectively. The current collector is abbreviated as CC.
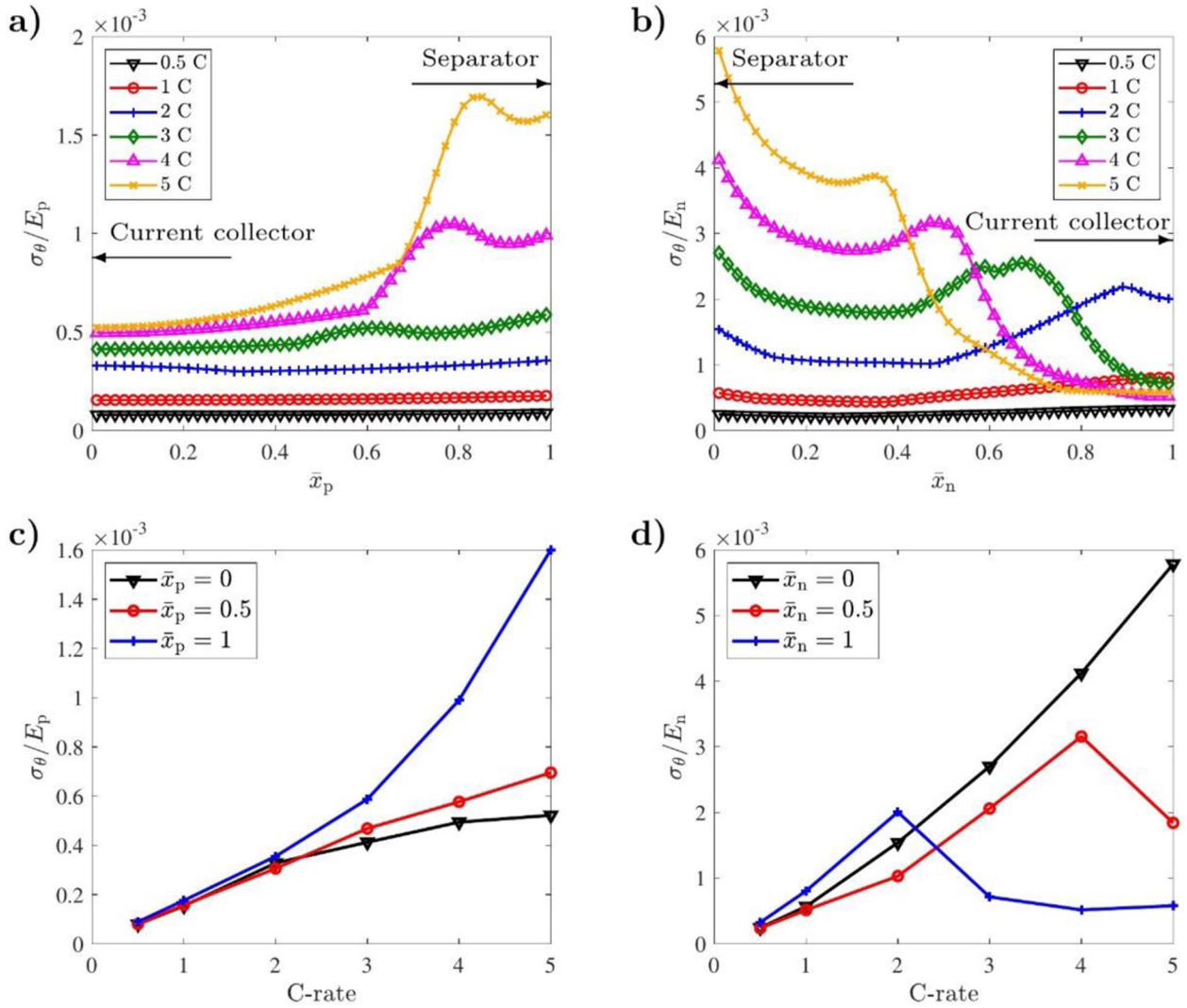
Figure 9. Maximum tangential stress at particle surface in electrodes at different C-rates of discharging: stress distribution in (a) cathode and (b) anode; and maximum stress versus C-rate at different locations in (c) cathode and (d) anode.

to analyse how mechanical stresses affect the degradation and lifetime of batteries, which will be considered in future work.

Appendix A: Dealing with Discontinuities Between the Electrodes and the Separator

The discontinuities at the interface between the electrodes and the separator were dealt with in the finite volume method by using the harmonic mean approach in LIONSIMBA.[49] Here, a brief description of the method is presented, details of which are referred to Ref. 49.

The last volume in the cathode, the first volume in the separator and the interface in between are depicted in Figure A1. The diffusion coefficient of the electrolyte at the interface is obtained using the harmonic mean as shown below

$$D_{\text{eff},k+\frac{1}{2}} = \frac{D_{\text{eff},k}D_{\text{eff},k+1}}{\beta D_{\text{eff},k+1} + (1-\beta)D_{\text{eff},k}} \qquad \text{[A1]}$$

Where $\beta = \frac{\Delta x_{\text{p}}}{\Delta x_{\text{p}} + \Delta x_{\text{s}}}$ and k is the index of volumes. The electrolyte diffusion equations in the two volumes are respectively

$$\epsilon_{\text{p}} \frac{\partial c_{\text{e},k}(t)}{\partial t} = D_{\text{eff},k+\frac{1}{2}} \frac{c_{\text{e},k+1}(t) - c_{\text{e},k}(t)}{\Delta x_{\text{p}} \Delta \tilde{x}} - D_{\text{eff},k-\frac{1}{2}} \frac{c_{\text{e},k}(t) - c_{\text{e},k-1}(t)}{(\Delta x_{\text{p}})^2} + \frac{1-t_+}{F} j^{\text{Li}}$$

$$\text{[A2]}$$

$$\epsilon_{\text{s}} \frac{\partial c_{\text{e},k+1}(t)}{\partial t} = D_{\text{eff},k+\frac{3}{2}} \frac{c_{\text{e},k+2}(t) - c_{\text{e},k+1}(t)}{(\Delta x_{\text{s}})^2} - D_{\text{eff},k+\frac{1}{2}} \frac{c_{\text{e},k+1}(t) - c_{\text{e},k}(t)}{\Delta x_{\text{s}} \Delta \tilde{x}} \qquad \text{[A3]}$$

where $\Delta \tilde{x} = \frac{\Delta x_{\text{p}} + \Delta x_{\text{s}}}{2}$. The same approach is applied to the interface between the anode and the separator and other interface conditions where needed.
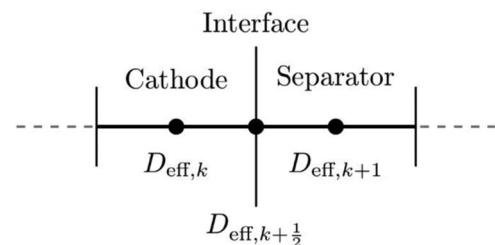

Figure A1. Dealing with the interface between cathode and separator in the electrolyte diffusion process.
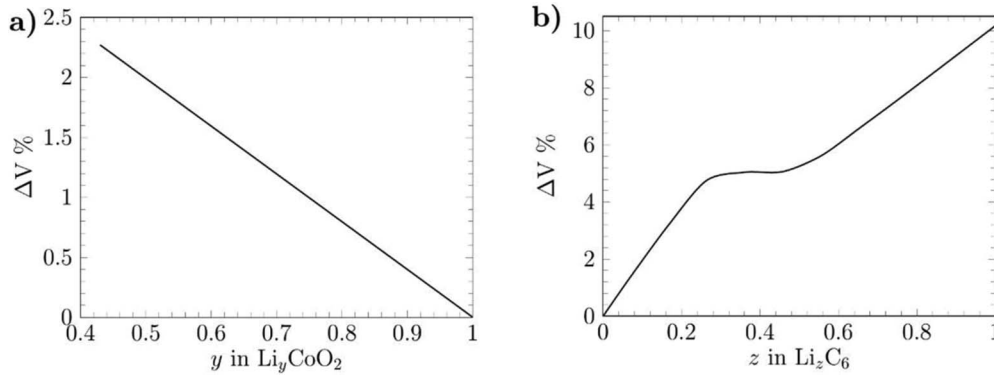
Figure B1. Volume change as a function of lithium stoichiometry in electrodes derived by X-ray diffraction measurements: (a) LCO cathode[54] and (b) graphite anode.[55]

Appendix B: Nonlinear Volume Change in Electrode Particles

The partial molar volume is defined as the volume change per mole of lithium in the electrode particles. This parameter was assumed to be constant in Ref. 16 for calculating stresses, while the partial molar volume was concentration-dependent in Ref. 33 for volume expansion. Here, the latter is used to predict the volume change of the pouch cell. For instance, the partial molar volume in the cathode and anode are respectively

$$\Omega_p(c) = \frac{\Delta V_{\mathrm{p}}(y)}{(y-1)\,c_{\mathrm{p,max}}}, \quad \Omega_n(c) = \frac{\Delta V_{\mathrm{n}}(z)}{z\,c_{\mathrm{n,max}}} \qquad [\mathrm{B1}]$$

where ΔV is the volume change in Figure B1, and y and z are the stoichiometric coefficients in cathode and anode respectively. The thickness in Equation 17 thus becomes

$$dL = \alpha_{\mathrm{cell}}(T - T_0) + n \cdot \left[\sum_{i=1}^{n_{\mathrm{p}}} \epsilon_{\mathrm{s}} L_i V_{\mathrm{p}}(y) + \sum_{i=1}^{n_{\mathrm{n}}} \epsilon_{\mathrm{s}} L_i V_{\mathrm{n}}(z) \right] \qquad [\mathrm{B2}]$$

Constant partial molar volumes are used for calculating stresses inside electrode particles to avoid numerical difficulties, where the values in Table III are approximately equal to the calculations by Equation B1 with $y = 0.43$ and $z = 0$.

List of Symbols

a_{s}	specific interfacial area (m^{-1})
c_i	concentration of lithium in phase i (mol m^{-3})
D_i	diffusion coefficient of ionic lithium in phase i (m^2 s^{-1})
k_i	reaction rate in phase i (m s^{-1})
i	electronic current (A)
L_i	thickness of domain i (m)
i_0	exchange current density (A m^{-2})
j^{Li}	reaction current density (A m^{-2})
R_i	particle radius in phase i (m)
R	universal gas constant (8.314 J mol^{-1} K^{-1})
F	Faraday constant (96485 C mol^{-1})
T	absolute temperature (K)
t_+^0	transference number of lithium-ion
A_{cell}	cell surface area (m^2)
L_{cell}	cell thickness (m)
V_{cell}	cell volume (m^3)
n	number of cathode and anode layers in the pouch cell
h_{conv}	convective heat transfer coefficient (W m^{-2} K^{-1})
q_{conv}	convective heat transfer rate (W)
q_{rad}	radiation heat transfer rate (W)
q_{tot}	heat generation rate in electrodes and separator (W)
$c_{\mathrm{p,cell}}$	cell heat capacity (J kg^{-1} K^{-1})
E_{OCV}	thermodynamic equilibrium potential (V)
E	Young's modulus (Pa)
ν	Poisson's ratio
brugg	Bruggeman's coefficient

Subscripts and Superscripts

p	positive electrode/cathode
sep	separator
n	negative electrode/anode
eff	effective parameter
avg	average parameter
surf	surface parameter
s	solid phase
e	electrolyte phase
CC	current collector
r	radial direction
θ	tangential direction
ref	reference
cell	parameter for the pouch cell
max	maximum value

Greek

ϕ_i	potential of phase i (V)
κ	conductivity of electrolyte (S m^{-1})
η	electrode surface overpotential (V)
ρ_{cell}	cell density (kg m^{-3})
α_{cell}	thermal expansion coefficient (μm K^{-1})
ϵ_{e}	volume fraction of electrolyte
ϵ_{s}	volume fraction of active material
ϵ_{rad}	emissivity
σ_{B}	Stefan-Boltzmann constant (5.6704$\times 10^{-8}$ W m^{-2} K^{-4})
Ω	partial molar volume (cm^3 mol^{-1})
σ	solid phase conductivity (S m^{-1})
σ_{r}	radial stress (Pa)
σ_θ	tangential stress (Pa)

ORCID

Weilong Ai https://orcid.org/0000-0003-2526-4654
Ludwig Kraft https://orcid.org/0000-0003-4324-426X
Johannes Sturm https://orcid.org/0000-0001-8876-9989
Andreas Jossen https://orcid.org/0000-0003-0964-1405
Billy Wu https://orcid.org/0000-0003-3963-4900

References

1. S. Müller, P. Pietsch, B. E. Brandt, P. Baade, V. De Andrade, F. De Carlo, and V. Wood, Quantification and modeling of mechanical degradation in lithium-ion batteries based on nanoscale imaging, *Nat. Commun.*, **9**, 1 (2018).
2. X. H. Liu, L. Zhong, S. Huang, S. X. Mao, T. Zhu, and J. Y. Huang, Size-dependent fracture of silicon nanoparticles during lithiation, *ACS Nano.*, **6**, 1522 (2012).
3. H. Wu, G. Chan, J. W. Choi, I. Ryu, Y. Yao, M. T. Mcdowell, S. W. Lee, A. Jackson, Y. Yang, L. Hu, and Y. Cui, Stable cycling of double-walled silicon nanotube battery anodes through solid-electrolyte interphase control, *Nat. Nanotechnol.*, **7**, 310 (2012).
4. F. Tariq, V. Yufit, D. S. Eastwood, Y. Merla, M. Biton, B. Wu, Z. Chen, K. Freedman, G. Offer, E. Peled, P. D. Lee, D. Golodnitsky, and N. Brandon, In-Operando X-ray Tomography Study of Lithiation Induced Delamination of Si Based Anodes for Lithium-Ion Batteries, *ECS Electrochem. Lett.*, **3**, A76 (2014).
5. A. Mukhopadhyay and B. W. Sheldon, Deformation and stress in electrode materials for Li-ion batteries, *Prog. Mater. Sci.*, **63**, 58 (2014).
6. M. R. Palacín and A. De Guibert, Batteries: Why do batteries fail?, *Science*, (80-.)., **351**, 1253292 (2016).

7. M. Ebner, F. Marone, M. Stampanoni, and V. Wood, Visualization and quantification of electrochemical and mechanical degradation in li-ion batteries, *Science*, (80-.)., **342**, 716 (2013).

8. Y. Merla, B. Wu, V. Yufit, N. P. Brandon, R. F. Martinez-Botas, and G. J. Offer, Novel application of differential thermal voltammetry as an in-depth state-of-health diagnosis method for lithium-ion batteries, *J. Power Sources.*, **307**, 308 (2016).

9. R. Deshpande, M. Verbrugge, Y.-T. Cheng, J. Wang, and P. Liu, Battery Cycle Life Prediction with Coupled Chemical Degradation and Fatigue Mechanics, *J. Electrochem. Soc.*, **159**, A1730 (2012).

10. D. Sauerteig, N. Hanselmann, A. Arzberger, H. Reinshagen, S. Ivanov, and A. Bund, Electrochemical-mechanical coupled modeling and parameterization of swelling and ionic transport in lithium-ion batteries, *J. Power Sources.*, **378**, 235 (2018).

11. A. Jana, G. M. Shaver, and R. E. García, Physical, on the fly, capacity degradation prediction of LiNiMnCoO2-graphite cells, *J. Power Sources.*, **422**, 185 (2019).

12. M. T. McDowell, S. Xia, and T. Zhu, The mechanics of large-volume-change transformations in high-capacity battery materials, *Extrem. Mech. Lett.*, **9**, 480 (2016).

13. Y. Zhao, P. Stein, Y. Bai, M. Al-siraj, Y. Yang, and B. Xu, Review article A review on modeling of electro-chemo-mechanics in lithium-ion batteries, *J. Power Sources.*, **413**, 259 (2019).

14. J. Christensen and J. Newman, A Mathematical Model of Stress Generation and Fracture in Lithium Manganese Oxide, *J. Electrochem. Soc.*, **153**, A1019 (2006).

15. J. Christensen and J. Newman, Stress generation and fracture in lithium insertion materials, *J. Solid State Electrochem.*, **10**, 293 (2006).

16. X. Zhang, W. Shyy, and A. Marie Sastry, Numerical Simulation of Intercalation-Induced Stress in Li-Ion Battery Electrode Particles, *J. Electrochem. Soc.*, **154**, A910 (2007).

17. J. Li, K. Adewuyi, N. Lotfi, R. G. Landers, and J. Park, A single particle model with chemical/mechanical degradation physics for lithium ion battery State of Health (SOH) estimation, *Appl. Energy.*, **212**, 1178 (2018).

18. R. Purkayastha and R. M. McMeeking, A Linearized Model for Lithium Ion Batteries and Maps for their Performance and Failure, *J. Appl. Mech.*, **79**, 031021 (2012).

19. M. Klinsmann, D. Rosato, M. Kamlah, and R. M. McMeeking, Modeling Crack Growth during Li Extraction in Storage Particles Using a Fracture Phase Field Approach, *J. Electrochem. Soc.*, **92**, 313 (2016).

20. Y. T. Cheng and M. W. Verbrugge, Evolution of stress within a spherical insertion electrode particle under potentiostatic and galvanostatic operation, *J. Power Sources.*, **190**, 453 (2009).

21. B. Suthar, P. W. C. Northrop, R. D. Braatz, and V. R. Subramanian, Optimal Charging Profiles with Minimal Intercalation-Induced Stresses for Lithium-Ion Batteries Using Reformulated Pseudo 2-Dimensional Models, *J. Electrochem. Soc.*, **161**, F3144 (2014).

22. L. Wu, Y. Wen, and J. Zhang, Three-Dimensional Finite Element Study on Li Diffusion Induced Stress in FIB-SEM Reconstructed LiCoO$_2$ Half Cell, *Electrochim. Acta.*, **222**, 814 (2016).

23. H. Mendoza, S. A. Roberts, V. E. Brunini, and A. M. Grillet, Mechanical and Electrochemical Response of a LiCoO$_2$ Cathode using Reconstructed Microstructures, *Electrochim. Acta.*, **190**, 1 (2016).

24. Y. T. Cheng and M. W. Verbrugge, The influence of surface mechanics on diffusion induced stresses within spherical nanoparticles, *J. Appl. Phys.*, 104 (2008).

25. T. R. Garrick, X. Huang, V. Srinivasan, and J. W. Weidner, Modeling Volume Change in Dual Insertion Electrodes, *J. Electrochem. Soc.*, **164**, E3552 (2017).

26. K. Smith and C. Y. Wang, Power and thermal characterization of a lithium-ion battery pack for hybrid-electric vehicles, *J. Power Sources.*, **160**, 662 (2006).

27. B. Wu, V. Yufit, Y. Merla, R. F. Martinez-Botas, N. P. Brandon, and G. J. Offer, Differential thermal voltammetry for tracking of degradation in lithium-ion batteries, *J. Power Sources.*, **273**, 495 (2015).

28. Y. Merla, B. Wu, V. Yufit, R. F. Martinez-Botas, and G. J. Offer, An easy-to-parameterise physics-informed battery model and its application toward lithium-ion battery cell design, diagnosis, and degradation, *J. Power Sources.*, **384**, 66 (2018).

29. C. Patsios, B. Wu, E. Chatzinikolaou, D. J. Rogers, N. Wade, N. P. Brandon, and P. Taylor, An integrated approach for the analysis and control of grid connected energy storage systems, *J. Energy Storage.*, **5**, 48 (2016).

30. G. J. Offer, V. Yufit, D. A. Howey, B. Wu, and N. P. Brandon, Module design and fault diagnosis in electric vehicle batteries, *J. Power Sources.*, **206**, 383 (2012).

31. J. Christensen, Modeling Diffusion-Induced Stress in Li-Ion Cells with Porous Electrodes, *J. Electrochem. Soc.*, **157**, A366 (2010).

32. R. Fu, M. Xiao, and S. Y. Choe, Modeling, validation and analysis of mechanical stress generation and dimension changes of a pouch type high power Li-ion battery, *J. Power Sources.*, **224**, 211 (2013).

33. B. Rieger, S. V. Erhard, K. Rumpf, and A. Jossen, A New Method to Model the Thickness Change of a Commercial Pouch Cell during Discharge, *J. Electrochem. Soc.*, **163**, A1566 (2016).

34. S. Renganathan, G. Sikha, S. Santhanagopalan, and R. E. White, Theoretical Analysis of Stresses in a Lithium Ion Cell, *J. Electrochem. Soc.*, **157**, A155 (2009).

35. B. Suthar, P. W. C. Northrop, D. Rife, and V. R. Subramanian, Effect of Porosity, Thickness and Tortuosity on Capacity Fade of Anode, *J. Electrochem. Soc.*, **162**, A1708 (2015).

36. B. Wu and W. Lu, A battery model that fully couples mechanics and electrochemistry at both particle and electrode levels by incorporation of particle interaction, *J. Power Sources.*, **360**, 360 (2017).

37. B. Rieger, S. V. Erhard, S. Kosch, M. Venator, A. Rheinfeld, and A. Jossen, Multi-Dimensional Modeling of the Influence of Cell Design on Temperature, Displacement and Stress Inhomogeneity in Large-Format Lithium-Ion Cells, *J. Electrochem. Soc.*, **163**, A3099 (2016).

38. V. Ramadesigan, P. W. C. Northrop, S. De, S. Santhanagopalan, R. D. Braatz, and V. R. Subramanian, Modeling and Simulation of Lithium-Ion Batteries from a Systems Engineering Perspective, *J. Electrochem. Soc.*, **159**, R31 (2012).

39. A. Jokar, B. Rajabloo, M. Désilets, and M. Lacroix, Review of simplified Pseudo-two-Dimensional models of lithium-ion batteries, *J. Power Sources.*, **327**, 44 (2016).

40. X. Hu, S. Li, and H. Peng, A comparative study of equivalent circuit models for Li-ion batteries, *J. Power Sources.*, **198**, 359 (2012).

41. B. Yann, G. Nagasubramanian, R. G. Jungst, and D. H. Doughty, Modeling of lithium ion cells — A simple equivalent-circuit model approach, *Solid State Ionics*, **175**, 835 (2004).

42. J. Newman and K. E. Thomas-Alyea, Electrochemical Systems, 2004.

43. M. Doyle and J. Newman, The use of mathematical modeling in the design of lithium/polymer battery systems, *Electrochim. Acta.*, **40**, 2191 (1995).

44. G. M. Goldin, A. M. Colclasure, A. H. Wiedemann, and R. J. Kee, Three-dimensional particle-resolved models of Li-ion batteries to assist the evaluation of empirical parameters in one-dimensional models, *Electrochim. Acta.*, **64**, 118 (2012).

45. R. E. Garcıá, Y.-M. Chiang, W. Craig Carter, P. Limthongkul, and C. M. Bishop, Microstructural Modeling and Design of Rechargeable Lithium-Ion Batteries, *J. Electrochem. Soc.*, **152**, A255 (2005).

46. B. Wu, V. Yufit, M. Marinescu, G. J. Offer, R. F. Martinez-Botas, and N. P. Brandon, Coupled thermal-electrochemical modelling of uneven heat generation in lithium-ion battery packs, *J. Power Sources.*, **243**, 544 (2013).

47. M. Guo, G. Sikha, and R. E. White, Single-Particle Model for a Lithium-Ion Cell: Thermal Behavior, *J. Electrochem. Soc.*, **158**, A122 (2011).

48. R. E. Rahimian, Saeed Khaleghi, and Rayman, Sean and White, Extension of physics-based single particle model for higher charge–discharge rates, *J. Power Sources.*, **224**, 180 (2013).

49. M. Torchio, L. Magni, R. B. Gopaluni, R. D. Braatz, and D. M. Raimondo, LIONSIMBA: A Matlab Framework Based on a Finite Volume Model Suitable for Li-Ion Battery Design, Simulation, and Control, *J. Electrochem. Soc.*, **163**, A1192 (2016).

50. Y. Troxler, B. Wu, M. Marinescu, V. Yu, Y. Patel, A. J. Marquis, N. P. Brandon, and G. J. Offer, The effect of thermal gradients on the performance of lithium-ion batteries, *J. Power Sources.*, **247**, 1018(2014).

51. J. Li, N. Lotfi, R. G. Landers, and J. Park, A Single Particle Model for Lithium-Ion Batteries with Electrolyte and Stress-Enhanced Diffusion Physics, *J. Electrochem. Soc.*, **164**, A874 (2017).

52. B. Rieger, S. Schlueter, S. V. Erhard, J. Schmalz, G. Reinhart, and A. Jossen, Multiscale investigation of thickness changes in a commercial pouch type lithium-ion battery, *J. Energy Storage.*, **6**, 213 (2016).

53. J. N. Reimers, Electrochemical and In Situ X-Ray Diffraction Studies of Lithium Intercalation in Li$_x$CoO$_2$, *J. Electrochem. Soc.*, **139**, 2091 (1992).

54. B. Rieger, S. Schlueter, S. V. Erhard, and A. Jossen, Strain Propagation in Lithium-Ion Batteries from the Crystal Structure to the Electrode Level, *J. Electrochem. Soc.*, **163**, A1595 (2016).

55. R. Yazami and Y. Reynier, Thermodynamics and crystal structure anomalies in lithium-intercalated graphite, *J. Power Sources.*, **153**, 312 (2006).

56. Y. Song, X. Shao, Z. Guo, and J. Zhang, Role of material properties and mechanical constraint on stress-assisted diffusion in plate electrodes of lithium ion batteries, *J. Phys. D. Appl. Phys.*, 46 (2013).

57. I. Laresgoiti, S. Käbitz, M. Ecker, and D. U. Sauer, Modeling mechanical degradation in lithium ion batteries during cycling: Solid electrolyte interphase fracture, *J. Power Sources.*, **300**, 112 (2015).

58. V. Malavé, J. R. Berger, H. Zhu, and R. J. Kee, A computational model of the mechanical behavior within reconstructed Li$_x$CoO$_2$ Li-ion battery cathode particles, *Electrochim. Acta.*, **130**, 707 (2014).